

# Conductivity in organic semiconductors hybridized with the vacuum field

E. Orgiu<sup>1†</sup>, J. George<sup>1†</sup>, J. A. Hutchison<sup>1†</sup>, E. Devaux<sup>1</sup>, J. F. Dayen<sup>2</sup>, B. Doudin<sup>2</sup>, F. Stellacci<sup>3</sup>, C. Genet<sup>1</sup>, J. Schachenmayer<sup>4</sup>, C. Genes<sup>5</sup>, G. Pupillo<sup>1,2</sup>, P. Samori<sup>1</sup> and T. W. Ebbesen<sup>1\*</sup>

**Much effort over the past decades has been focused on improving carrier mobility in organic thin-film transistors by optimizing the organization of the material or the device architecture. Here we take a different path to solving this problem, by injecting carriers into states that are hybridized to the vacuum electromagnetic field. To test this idea, organic semiconductors were strongly coupled to plasmonic modes to form coherent states that can extend over as many as  $10^5$  molecules and should thereby favour conductivity. Experiments show that indeed the current does increase by an order of magnitude at resonance in the coupled state, reflecting mostly a change in field-effect mobility. A theoretical quantum model confirms the delocalization of the wavefunctions of the hybridized states and its effect on the conductivity. Our findings illustrate the potential of engineering the vacuum electromagnetic environment to modify and to improve properties of materials.**

Light and matter can enter into the strong-coupling regime by exchanging photons faster than any competing dissipation processes. This is normally achieved by placing the material in a confined electromagnetic environment, such as a Fabry–Perot cavity composed of two parallel mirrors that is resonant with an electronic transition in the material. Alternatively, one can use surface plasmon resonances, as in this study. Strong coupling leads to the formation of two hybridized light–matter polaritonic states,  $P+$  and  $P-$ , separated by the so-called Rabi splitting, as illustrated in Fig. 1a. According to quantum electrodynamics, in the absence of dissipation, the Rabi splitting for a single molecule is given by

$$\hbar\Omega_R = 2\sqrt{\frac{\hbar\omega}{2\epsilon_0\nu}} \cdot d \cdot \sqrt{n_{\text{ph}} + 1} \quad (1)$$

where  $\hbar\omega$  is the cavity resonance or transition energy ( $\hbar$  the reduced Planck constant),  $\epsilon_0$  the vacuum permittivity,  $\nu$  the mode volume,  $d$  the transition dipole moment of the material and  $n_{\text{ph}}$  the number of photons present in the system. The last term in equation (1) implies that, even in the dark, the Rabi splitting has a finite value owing to the interaction with the vacuum electromagnetic field. This vacuum Rabi splitting can be further increased by coupling a large number  $N$  of oscillators to the electromagnetic mode, as  $\hbar\Omega_R^N \propto \sqrt{N}$  (ref. 1). In this ensemble coupling, in addition to  $P+$  and  $P-$ , there are many other combinations of states, known as dark states<sup>2</sup>, that are located in the middle of the Rabi splitting, as illustrated in Fig. 1a.

Polaritons have been extensively studied in inorganic and organic materials<sup>3–25</sup>. Vacuum Rabi splittings as large as 1 eV have been reported for strongly coupled molecules<sup>6,7</sup>, thereby significantly modifying the electronic structure of the molecular material, as can be seen in the work function, the ground state energy shift, and the chemical reactivity<sup>8–10</sup>. In such situations,  $P+$  and  $P-$  are coherent collective states (Fig. 1b) that extend over the mode volume and may involve  $\sim 10^5$  oscillators, as in the present systems.

This collective nature has been demonstrated by the coherent fluorescence of  $P-$  over distances of micrometres in strongly coupled molecular states<sup>11,25</sup>.

Organic semiconductors have generated considerable interest due to their potential to create inexpensive and flexible devices that are easily processed on a large scale<sup>26–36</sup>. However, technological applications are at present limited by the low mobility of the charge carriers, which is associated with the disorder in these materials<sup>30–33</sup>. Hence, charge carrier mobility in organic semiconductors should also benefit from the extended coherence associated with light-hybridized states as compared to the normal carrier mobilities limited by the hopping between molecules and by scattering induced by molecular disorder.

Although electron-injected polariton LEDs and lasers have been reported in recent years<sup>18–23</sup>, conductivity mediated by light-hybridized materials has not been considered. One of the challenges in those studies has been to inject electrons into  $P+$  or  $P-$ , as these states have not just well-defined energies but also well-defined momenta associated with their dispersion curves. In this regard, molecular materials have the advantage that the energies of the states are inhomogeneously broadened and fluctuating in time, resulting in spectral widths that facilitate polariton creation. Indeed the very first study of polariton electroluminescence was carried out on organic materials<sup>24</sup>.

In this study, an initial screening was carried out on different organic semiconductors known to be air stable and exhibit good field-effect mobilities in solution-processed devices ( $10^{-2}$ – $10^{-1}$  cm<sup>2</sup> V<sup>-1</sup> s<sup>-1</sup> for optimized field-effect geometries). We focus here on three members of the aromatic diimide family, an example of which, PDI2EH-CN<sub>2</sub>, is shown in Fig. 1c (refs 34–36). The synthesis of this molecule is described in Supplementary Section I. The other molecules are the brominated version of the former, PDI2EH-BR<sub>2</sub>, and the diimide naphthalene polymer, P(NDI2OD-T2) (ActivInk N2200 from Polyera). Note that we

<sup>1</sup>ISIS & icFRC, Université de Strasbourg and CNRS, 67000 Strasbourg, France. <sup>2</sup>IPCMS & icFRC, Université de Strasbourg and CNRS, 67034 Strasbourg, France. <sup>3</sup>EPFL, STI SMX-GE MXG O30 Station 12, CH-1015 Lausanne, Switzerland. <sup>4</sup>JILA, NIST, Department of Physics, University of Colorado, 440 UCB, Boulder, Colorado 80309, USA. <sup>5</sup>Institut für Theoretische Physik, Universität Innsbruck, Technikerstrasse 25, A-6020 Innsbruck, Austria. <sup>†</sup>These authors contributed equally to this work. \*e-mail: ebbesen@unistra.fr

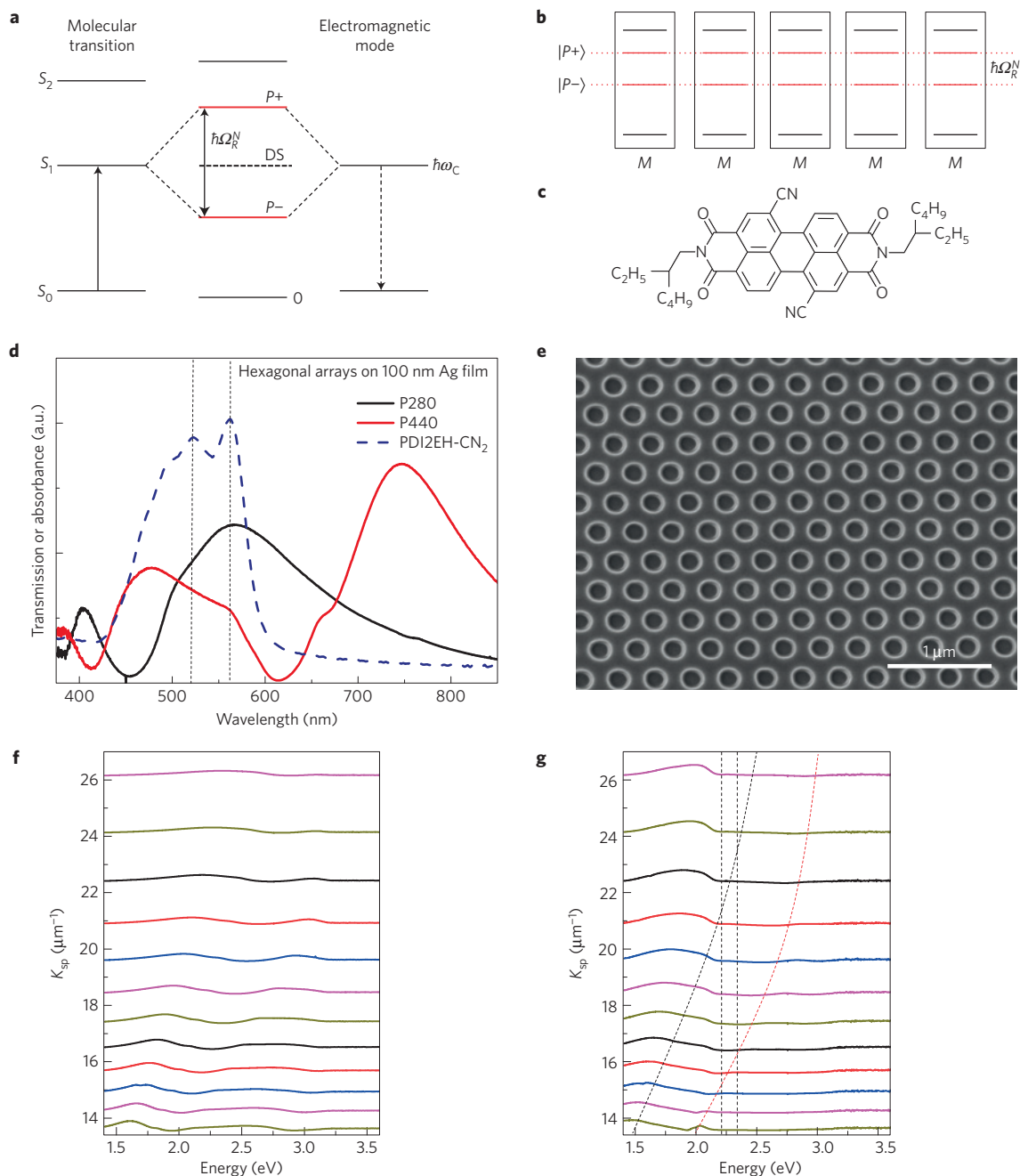


**Figure 1 | Light-matter strong coupling with organic semiconductors.** **a**, Illustration of the strong coupling between a molecular electronic transition ( $S_0$  to  $S_1$ ) and an optical cavity mode of the same energy ( $\hbar\omega_C$ ). Two new hybrid light-matter states  $P+$  and  $P-$  are formed, separated by the Rabi splitting  $\hbar\Omega_R^N$ . The energy level of the so-called dark states (DS) is also indicated. **b**, Illustration of the collective nature  $P+$  and  $P-$ , forming a coherent state involving many molecules or molecular units ( $M$ ). **c**, Molecular structure of PDI2EH-CN<sub>2</sub>. **d**, Absorbance spectra of a thin film of PDI2EH-CN<sub>2</sub> (dashed blue) and examples of resonances of two hole arrays whose resonance matches the centre of the molecular absorbance. **e**, Electron microscope image of a hexagonal array milled in a Al metal film which provides the surface plasmon resonance that is strongly coupled to the molecule. **f, g**, Dispersion of the surface plasmon modes in the absence (**f**) and presence (**g**) of PDI2EH-CN<sub>2</sub> as a function of the period  $P$  every 20 nm between 240 nm (top curve) and 460 nm (bottom curve). In **g**, the dashed lines are guides to the eye, with the vertical lines indicating the position of the PDI2EH-CN<sub>2</sub> absorption peaks shown in **d** and the curved lines indicating the shift in the plasmon resonances.

have chosen these organic materials in view of their very different charge transport capacities, but also because they all possess a lowest unoccupied molecular orbital (LUMO) energy level at  $\sim 4$  eV (see Supplementary Section IV). This last observation rules out the injection capacity as a main parameter for the interpretation of the results appearing later in the manuscript when comparing their relative response. Instead, as we will see, the differences that are important are the intrinsic charge transport capacity of

each molecular system, influenced by the film disorder. These compounds possess intense absorption bands (Fig. 1d) that can be used to strongly couple them to surface plasmon resonances. For this we used a hexagonal array of holes (Fig. 1e), in either Al or Ag films, which give rise to well-defined surface plasmon resonances<sup>37,38</sup>, also shown in Fig. 1d. The low work function of an Al electrode is generally favourable for electron injection in n-type semiconductors. In the case of a Ag electrode, we still have

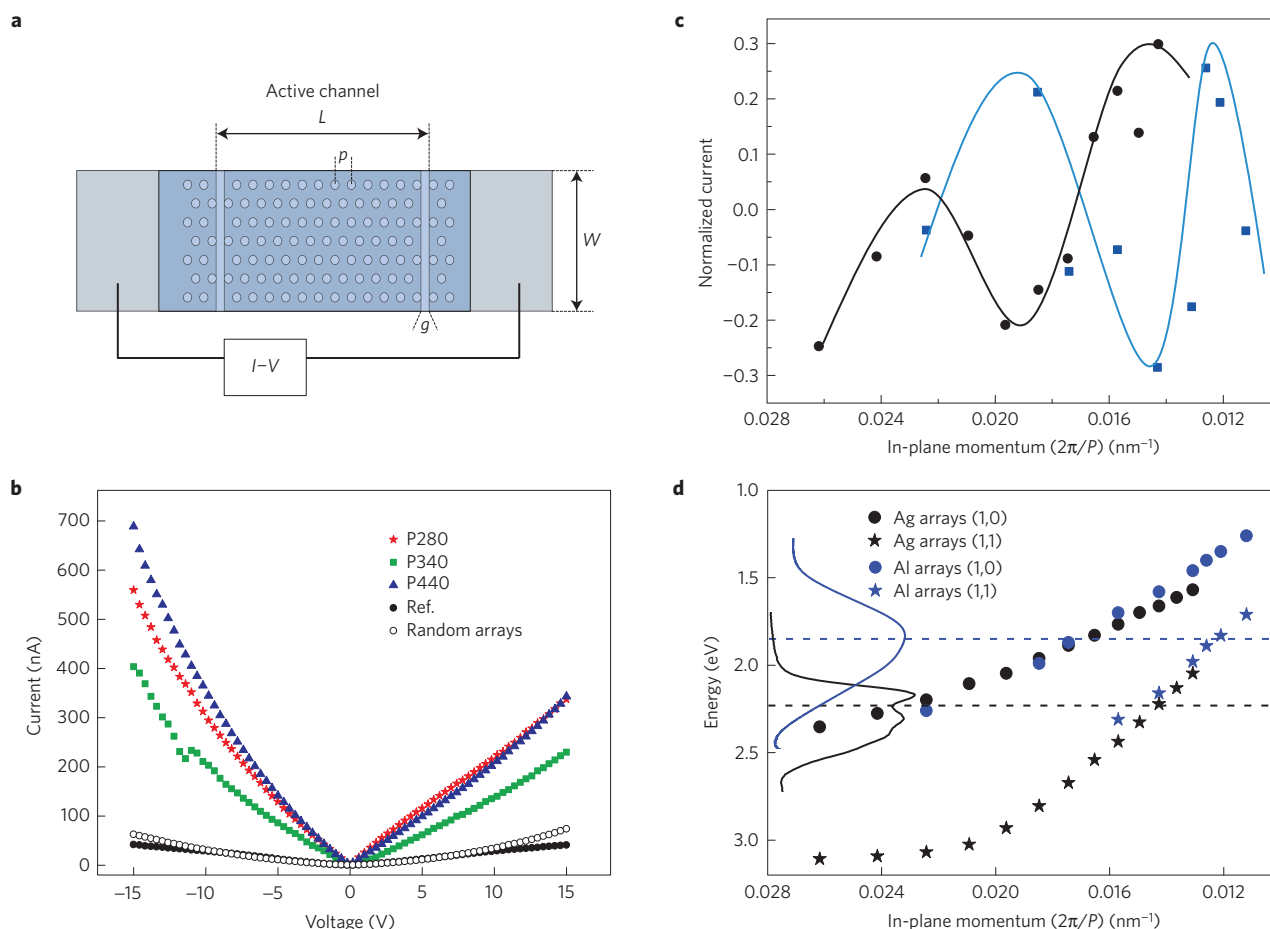


**Figure 2 | Conductivity measurements under strong coupling on Ag and Al arrays.** **a**, Illustration of the configuration used to measure conductivity using surface plasmon resonances generated by the hexagonal array milled in a 100-nm-thick Ag film, 50  $\mu\text{m}$  wide, deposited on a glass substrate. The distance between the electrodes is 50  $\mu\text{m}$ . PDI2EH-CN<sub>2</sub> was spin-coated or evaporated, forming a 100-nm-thick layer on the array. The hole diameter is half the period. The gap between the array and the electrodes is 200 nm. **b**,  $I$ - $V$  curves as a function of the hexagonal array at selected periods for the configuration shown in **a**. **c**, Current measured at  $\pm 15$  V plotted as a function of period  $2\pi/P$  for PDI2EH-CN<sub>2</sub> (black circles, average of three data sets, each set being mean-centred and mean-normalized) and P-NDI2OD-T<sub>2</sub> (blue circles, average of two data sets, each set being mean-centred and mean-normalized) showing two distinct resonances. The black and blue solid lines are guides to the eye. **d**, The two resonances seen in the current of **c** correspond to the intersection of the molecular absorbance and the array plasmon resonance for the (1,0) and (1,1) modes of Ag (black) and Al (blue) arrays on the substrate side. The horizontal dashed lines are guides to the eye to show where the molecular absorbances intersect with the plasmon modes where the strong coupling occurs.

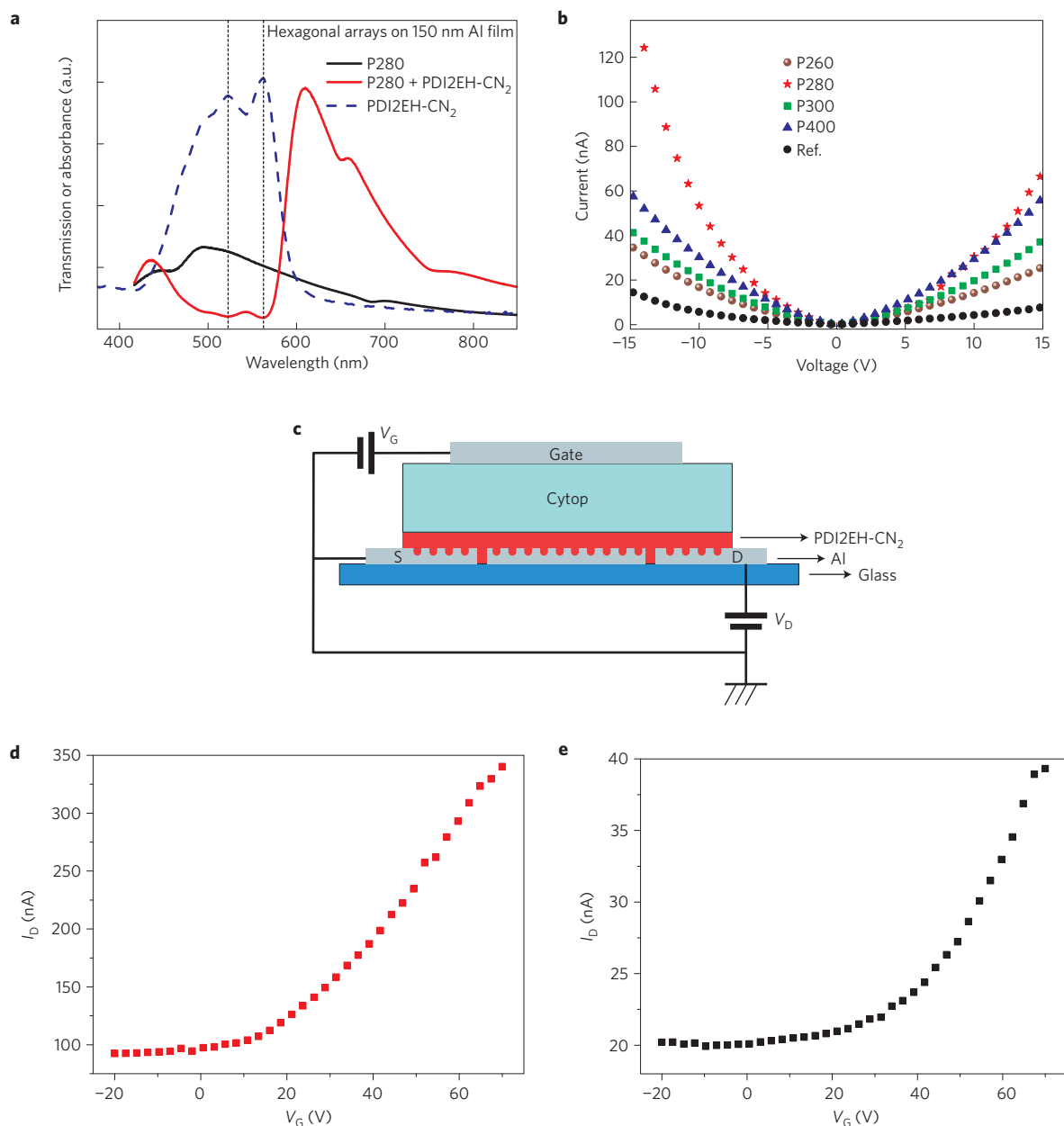
good electron injection, as confirmed in our experiments (see Supplementary Section IV, Supplementary Fig. 6). Such efficient electron injection from metals with a high work function into PDI derivatives has been previously reported<sup>34,36</sup>.

Figure 1f,g shows, respectively, the dispersion of surface plasmon resonances of the Ag hole array as a function of hole period in the bare state and when the array is covered with a thin film of PDI2EH-CN<sub>2</sub>. Unlike with Fabry-Perot cavities, in the case of strong coupling with surface plasmons on hole arrays the upper polariton is less visible owing to Fano-type interference<sup>6</sup>. However, a Rabi splitting of  $\sim 0.7$  eV can be estimated, corresponding to 30% of the transition energy, typical of the ultra-strong-coupling regime<sup>6,7</sup>.

To assess the conductivity of strongly coupled organic semiconductors, we compare it to that of the bare molecular material, by recording current-voltage ( $I$ - $V$ ) curves for thin films of the semiconductors between two electrodes, as illustrated in Fig. 2a. First, a 100-nm-thick layer of Al or Ag was evaporated on a glass substrate through a shadow mask to yield a long 80- $\mu\text{m}$ -wide strip. Then hexagonal arrays with period  $P$  were milled over a 55- $\mu\text{m}$ -long area on the metal strip. The active channel, 50  $\mu\text{m}$  long, was defined by milling gaps  $g$  of 200 nm separating this area from the source

and drain electrodes (Fig. 2a). The width of these gaps was found to be very important, because a distance larger than the decay of the evanescent field ( $\sim$  the wavelength) of the surface plasmon would result in the current flowing through an area where the material would not be hybridized. Note that the array continues for a few micrometres on both electrodes to ensure that the current is already injected into the strongly coupled system before reaching the active channel (Fig. 2a).

The  $I$ - $V$  curves were then recorded for different array periods and compared to that of an unstructured metal film also covered with the organic semiconductors (the reference). An example is shown for selected periods in Fig. 2b in the case of the PDI2EH-CN<sub>2</sub>. Similar experiments were carried out for the other two compounds. By plotting the current average at  $\pm 15$  V versus  $2\pi/P$ , with  $P$  being the period of the array, two current resonances are clearly visible, as can be seen in Fig. 2c for both PDI2EH-CN<sub>2</sub> and P(NDI2OD-T<sub>2</sub>). Interestingly, the current peaks occur for different periods. These correspond exactly to the intersections of the molecular absorption peaks and the surface plasmon modes (1,0) and (1,1) of the substrate side of the hole array where strong coupling occurs (Fig. 2d). In other words, the current is boosted when the organic



**Figure 3 | Conductivity under strong coupling on Al arrays and gating.** **a**, Spectra of Al hole arrays with and without PDI2EH-CN<sub>2</sub> as indicated. **b**,  $I$ - $V$  curves for selected periods versus reference in the same geometry as in Fig. 2a. **c**, Three-terminal gating device geometry, composed of: Al (40 nm) acting as a top gate;  $\sim 600$  nm of Cytosol, a polymer dielectric acting as a gate insulator ( $\epsilon_r = 2.1$ ); 100 nm of PDI2EH-CN<sub>2</sub> as the semiconductor layer; Al electrodes and nanohole array structure ( $W = 50 \mu\text{m}$ ,  $L = 50 \mu\text{m}$ ,  $V_D = +60$  V). Note that the surface plasmon modes are only slightly modified by the presence of the dielectric, as most of the evanescent plasmonic field is confined within the organic semiconductor layer. **d, e**, Typical transfer characteristics ( $I_D$ - $V_G$ ) of top-gate bottom-contact FETs realized on the structure proposed in Fig. 3c. In particular the graphs show the difference between a gated structure with hole arrays of periodicity  $P = 280$  nm (**d**) versus a reference structure with the same geometry but without nanohole arrays (**e**). The ratio of the mobilities is  $\mu_{\text{FET}(P=280\text{nm})} / \mu_{\text{FET}(\text{reference})} \sim 10$ , which corresponds essentially to the ratio of the current measured in the  $I$ - $V$  curves.

semiconductor is strongly hybridized with the surface plasmon modes. The current increases by over an order of magnitude in this regime. The third compound, PDI2EH-Br<sub>2</sub>, showed no detectable change in current with conductivity in the pA range (see Supplementary Fig. 5). The differences between these compounds will be discussed below. The widths of the conductivity resonances observed in Fig. 2c reflect the widths of both the absorbance of the semiconductor and the plasmon resonance. For that reason, a true off-resonance with periodic arrays is hard to achieve, weakening the contrast between the conductivity minima and maxima with respect to what would be observed if the semiconductor and plasmon

resonances were sharper. Please note that, in Fig. 2c, Ag and Al were chosen as the metal electrodes because, in each case, the charge injection is optimal for each electrode/semiconductor combination (see Supplementary Section IV). In addition, the injection from different metals was tested for PDI2EH-CN<sub>2</sub> and P(NDI2OD-T2), as reported in the Supplementary Fig. 2 for PDI2EH-CN<sub>2</sub> and Supplementary Fig. 6 for P(NDI2OD-T2).

The reference in the above data is always the unstructured metal film covered with the organic semiconductors. This reference shows a current larger than just the semiconductor, enhanced by the metallic substrate, but not shorted by the metal. Indeed, the

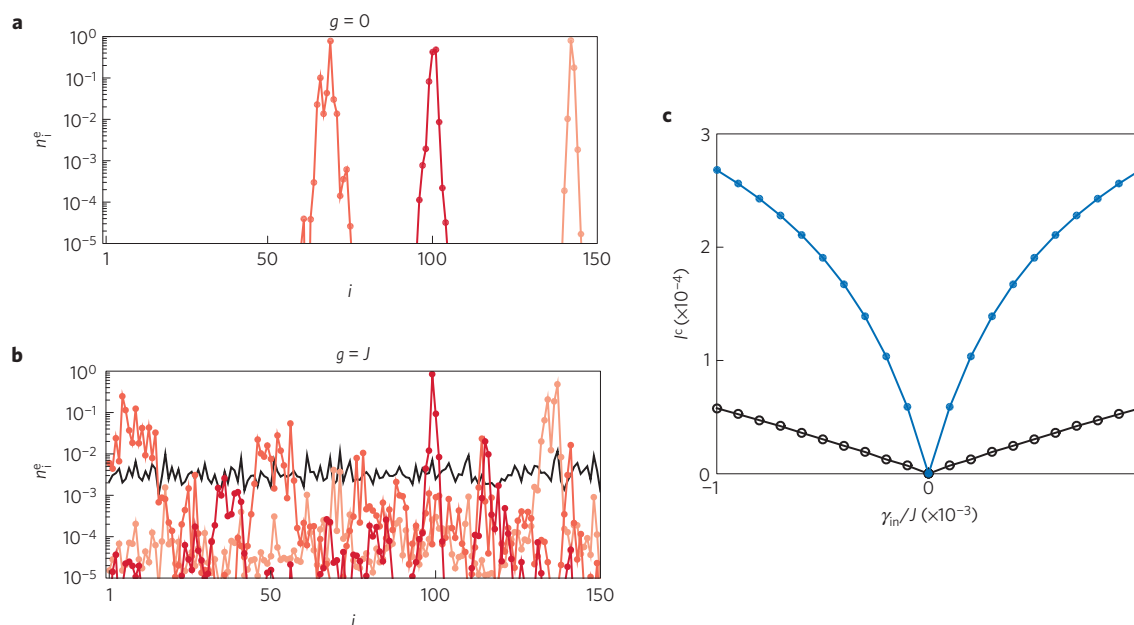


**Figure 4 | Theoretical model.** **a**, Electron density  $n_i^e$  as a function of the site (molecule) position  $i$ , for a chain of  $M=150$  molecules, in the presence of disorder (see text) and in the absence of plasmon-molecule coupling  $g=0$ . Because of disorder,  $n_i^e$  is localized at individual sites, as expected. **b**,  $n_i^e$  versus  $i$  for a finite plasmon-molecule coupling  $g=J$  in the strong-coupling regime. Surprisingly, electronic wavefunctions (and thus  $n_i^e$ ) become delocalized over the length of the sample. Black line: lower polariton. Other continuous lines:  $n_i^e$  corresponding to those of **a**. The three red/orange shades in **a** and **b** represent the same eigenstates in the absence and presence of coupling to the vacuum field, respectively. The solid lines connecting the points are guides for the eye. **c**, Electronic current  $I^e$  versus rate of electron pumping  $\gamma_{in}$ , analogous to  $I$ - $V$  curves for a chain with  $M=30$  molecules. Black open circles and blue filled circles correspond to the cases  $g=0$  and  $g=J$ , respectively.

measured field-effect mobility results from the intrinsic organic semiconducting properties. We have also checked random arrays of holes, which show no current increase (Fig. 2b), in agreement with expectations, as there are no well-defined plasmon resonances in such systems<sup>39</sup>.

In the case of PDI2EH-CN<sub>2</sub>, the same experiment was repeated on hexagonal hole arrays milled in an Al film with the spectra shown in Fig. 3a. The system shows (Fig. 3b) the strongest current resonance for a period of 280 nm, which again corresponds to the strongly coupled condition. The current increases by roughly an order of magnitude as compared to the reference consisting of PDI2EH-CN<sub>2</sub> on a flat Al film. To further assess the electronic properties of the coupled system, a three-terminal gated configuration was prepared, as illustrated schematically in Fig. 3c. Figure 3d,e shows the current versus the gating voltage for the on-resonance sample in Al and the reference, respectively. The mobility extracted from this data shows an increase from  $2.0 \times 10^{-3} \text{ cm}^2 \text{ V}^{-1} \text{ s}^{-1}$ —a value in agreement with the values extracted in a standard geometry (see Supplementary Table 1)—to  $1.7 \times 10^{-2} \text{ cm}^2 \text{ V}^{-1} \text{ s}^{-1}$ . In other words the increased carrier mobility in the coupled system is responsible for most of the enhanced current.

To explain the above results, we introduced a simple theoretical model where each molecule is represented by two states forming the conduction and valence bands of the semiconductor. The molecular states are resonantly coupled by the vacuum field with the relevant Hamiltonian

$$H = \left( - \sum_{j=1}^{M-1} J_j^e (c_j^e)^\dagger c_{j+1}^e - \sum_{j=1}^{M-1} J_j^h (c_j^h)^\dagger c_{j+1}^h + \sum_j g_j a^\dagger c_j^e c_j^h + \text{h.c.} \right) + \sum_{j=1}^M (\epsilon_j^e n_j^e + \epsilon_j^h n_j^h) \quad (2)$$

Here, in a second-quantized formalism,  $c_j^e (c_j^{e\dagger})$  and  $c_j^h (c_j^{h\dagger})$  correspond to the destruction (creation) of an electron in the conduction band and of a hole in the valence band, respectively, with  $n_j^e = c_j^{e\dagger} c_j^e$  ( $n_j^h = c_j^{h\dagger} c_j^h$ ) the local electron (hole) occupation, and  $j$  the site index (that is, the molecule location) for a system of size  $M$ , where  $M$  corresponds to the number of molecules. The local coupling  $g_j \propto d_{eh} \exp(-ik\ell j)$  (with strength  $d_{eh}$ ) is mediated by the surface plasmon field (with a delocalized surface plasmon wavevector  $k$ ) resonant with the interband transition<sup>20,40</sup>, here represented by a destruction (creation) operator  $a (a^\dagger)$ .  $\ell$  is the intermolecular spacing, in the nanometre range, and thus  $k\ell \ll 1$ . The third term represents processes where a surface plasmon is coherently created when an electron is transferred from the conduction to the valence band ( $a^\dagger c_j^e c_j^h$ ) and, vice versa, where a surface plasmon is coherently absorbed when an electron is promoted from the valence to the conduction band ( $c_j^{e\dagger} c_j^h a$ ). The last term represents possible local shifts of the energy  $\epsilon_j^e$  ( $\epsilon_j^h$ ) for the electrons (holes), arising, for example, because of disorder.

The two-band Hamiltonian equation (2) is reminiscent of the well-known Jaynes-Cummings model; however it takes into account the dynamics of electrons and holes. The terms  $J_j^e$  and  $J_j^h$  represent the quantum mechanical tunnelling rates of the charged particles between neighbouring sites. In the absence of disorder ( $J_j^e = J^e$ ,  $\epsilon_j^e = \epsilon^e$  and  $J_j^h = J^h$ ,  $\epsilon_j^h = \epsilon^h$  for all  $j$ ) and for  $g_j \simeq g=0$ , the first two terms in equation (2) imply extended Bloch-type wavefunctions for electrons and holes, which can in principle lead to a finite conductivity even at zero temperature. However, disorder in semiconductors in one dimension is known to invariably lead to wavefunction localization and vanishing conductivity<sup>41</sup>. Indeed, this is shown in Fig. 4a for  $g=0$ , where the probability density of a few chosen electronic states is shown to be exponentially localized for a situation where we have chosen disordered hopping rates  $J_j^{e,h} = J + \delta J_j^{e,h}$  and energy shifts  $\epsilon_j^{e,h} = \epsilon + \delta \epsilon_j^{e,h}$ , with  $\delta J_j^{e,h}$  and  $\delta \epsilon_j^{e,h}$  sets of random values (see Supplementary Section VI).

On coupling the system to the vacuum electromagnetic field, it is expected that polaritonic states delocalized throughout the mode volume should appear<sup>42,43</sup>. This is shown in Fig. 4b (black curve) for  $g = J$ , where, remarkably, the electronic component of the polaritonic density is shown to be delocalized despite the strong disorder. This value for  $g$  was chosen so that the collective coupling  $g\sqrt{M}$  is larger than all other coherent and incoherent rates, allowing the strong-coupling regime to be reached (see Supplementary Section VI). Surprisingly, in addition to the polaritonic state we find that under conditions of strong coupling also other electronic states in the conduction band of the model are modified by the hybridization with the vacuum field and can become delocalized over the same length of the sample, as shown in Fig. 4b for three eigenstates. This should have a considerable impact on conductivity, which we investigate next.

To probe the dynamics, we solve the master equation for the full density matrix of the system (see Supplementary Section VI) in the limit of low charge density. To mimic experiments, the master equation includes dissipative processes such as spontaneous decay of the plasmon mode and dephasing of the electron and hole wavefunctions—arising, for example, from local molecular vibrations. Electrons are incoherently pumped into the system at a rate  $\gamma_p$ , similar to the effects of an applied voltage. Figure 4c shows the equivalent of the  $I$ - $V$  curves derived from this model for  $M = 30$  sites and both  $g = 0$  and  $g = J$ . As can be seen, the current increases significantly in the presence of strong coupling. In Supplementary Section VI we show that in fact significant enhancement is obtained only in the strong-coupling regime, where the electronic wavefunctions hybridized with light are delocalized.

Despite its simplicity, the model clearly shows that the origin of the enhanced mobility under strong coupling can be explained by the extended coherence of the states induced by the hybridization with the vacuum field. This occurs over lengths that correspond to the mode volume (on the scale of the wavelength of the resonance), in contrast with the normal situation where the carrier is mostly confined to the molecular (or a few molecules) scale, in particular at room temperature.

It is important to note that, like for all conductors, disorder can strongly hinder charge transport whatever the transport mechanism. This is clearly shown in the case of PDI2EH-Br<sub>2</sub>, which has a similar molecular structure to PDI2EH-CN<sub>2</sub>, but a much lower mobility<sup>36</sup> as a result of disorder. We found extremely weak resonant enhancement, if any, despite the strong coupling (see Supplementary Fig. 5). The P(NDI2OD-T2) polymer presents an intermediate case where, despite the lower conductivity, the latter is enhanced by strong coupling. This is also confirmed by the model in the presence of large disorder, where, although the relative improvement of conductivity increases with disorder strength for a fixed light coupling  $g$  over the case  $g = 0$ , the overall conductivity tends to vanish.

The enhanced currents and the improved mobilities reported here demonstrate the potential of strong coupling for boosting conductivity in organic semiconductors. It is worth noting that at the same time the semiconducting properties are preserved. Although we used surface plasmon resonances to couple to the organic semiconductors, metal micro-cavities or dielectric resonators could also be used provided that the mode volumes are sufficiently small such that the strong-coupling condition can be met. In particular metallic Fabry–Perot cavities lead to even larger Rabi splittings than plasmonic arrays, which is important to increase the fraction of coupled oscillators in the sample, as we have shown elsewhere<sup>10</sup>. The challenge, we have found, is to ensure that there is no leakage via the top mirror when measuring the current parallel to the cavity.

Conductivity of strongly coupled systems can be implemented with ease in a variety of designs and configurations, including in plastics, depending on the application. Finally, our results show the importance of engineering the electromagnetic environment of

a material, not just for optical purposes, but also as a means to modify its properties through the formation of hybrid light–matter states. This opens new prospects for materials science as well as device technology.

**Note added in proof:** Since the submission of this work, two theoretical works have addressed the question of suppression of backscattering of conduction electrons for a two-dimensional electron gas off-resonantly coupled to a high-frequency classical electromagnetic field<sup>44,45</sup>.

## Methods

Methods and any associated references are available in the [online version of the paper](#).

Received 17 October 2014; accepted 21 July 2015;  
published online 14 September 2015

## References

- Haroche, S. in *Fundamental Systems in Quantum Optics* (eds Dalibard, J., Raimond, J. M. & Zinn-Justin, J.) (North Holland, 1992).
- Houdré, R. Early stage of continuous wave experiments on cavity-polaritons. *Phys. Status Solidi B* **242**, 2167–2196 (2005).
- Vasa, P. *et al.* Real-time observation of ultrafast Rabi oscillations between excitons and plasmons in metal nanostructures with J-aggregates. *Nature Photon.* **7**, 128–132 (2013).
- Agranovich, V. M. & Malshukov, A. G. Surface polariton spectra if the resonance with the transition layer vibrations exist. *Opt. Commun.* **11**, 169–171 (1974).
- Strashko, A. A. & Agranovich, V. M. To the theory of surface plasmon-polaritons on metals covered with resonant thin films. *Opt. Commun.* **332**, 201–205 (2014).
- Schwartz, T., Hutchison, J. A., Genet, C. & Ebbesen, T. W. Reversible switching of ultra-strong coupling. *Phys. Rev. Lett.* **106**, 196405 (2011).
- Kéna-Cohen, S., Maier, S. A. & Bradley, D. D. C. Ultrastrongly coupled exciton-polaritons in metal-clad organic semiconductor microcavities. *Adv. Opt. Mater.* **1**, 827–833 (2013).
- Hutchison, J. A., Schwartz, T., Genet, C., Devaux, E. & Ebbesen, T. W. Modifying chemical landscapes by coupling to the vacuum fields. *Angew. Chem. Int. Ed.* **51**, 1592–1596 (2012).
- Hutchison, J. A. *et al.* Tuning the work-function via strong coupling. *Adv. Mater.* **25**, 2481–2485 (2013).
- Canaguier-Durand, A. *et al.* Thermodynamics of molecules strongly coupled to the vacuum field. *Angew. Chem. Int. Ed.* **52**, 10533–10536 (2013).
- Abera Guebrou, S. *et al.* Coherent emission from a disordered organic semiconductor induced by strong coupling to surface plasmons. *Phys. Rev. Lett.* **108**, 066401 (2012).
- Deng, H., Haug, H. & Yamamoto, Y. Exciton-polariton Bose-Einstein condensation. *Rev. Mod. Phys.* **82**, 1490–1537 (2010).
- Kasprzak, J. *et al.* Bose-Einstein condensation of exciton polaritons. *Nature* **443**, 409–414 (2006).
- Kéna-Cohen, S. & Forrest, S. R. Room-temperature polariton lasing in an organic single-crystal microcavity. *Nature Photon.* **4**, 371–375 (2010).
- Ballarini, D. *et al.* All-optical polariton transistor. *Nature Commun.* **4**, 1778 (2013).
- Tanese, D. *et al.* Polariton condensation in solitonic gap states in a one-dimensional periodic potential. *Nature Commun.* **4**, 1749 (2013).
- Plumhof, J. D., Stöferle, T., Mai, L., Scherf, U. & Mahr, R. F. Room-temperature Bose-Einstein condensation of cavity exciton-polaritons in a polymer. *Nature Mater.* **13**, 247–252 (2014).
- Sapienza, L. *et al.* Electrically injected cavity polaritons. *Phys. Rev. Lett.* **100**, 136806 (2008).
- De Liberato, S. & Ciuti, C. Quantum theory of electron tunneling into intersubband cavity polariton states. *Phys. Rev. B* **79**, 075317 (2009).
- González-Tudela, A., Huidobro, P. A., Martín-Moreno, L., Tejedor, C. & García-Vidal, F. J. Theory of strong coupling between quantum emitters and propagating surface plasmons. *Phys. Rev. Lett.* **110**, 126801 (2013).
- Tsintzos, S. I., Pelekanos, N. T., Konstantinidis, G., Hatzopoulos, Z. & Savvidis, P. G. A GaAs polariton light-emitting diode operating near room temperature. *Nature* **453**, 372–375 (2013).
- Bhattacharya, P., Xiao, B., Bhowmick, S. & Heo, J. Solid state electrically inject exciton-polariton laser. *Phys. Rev. Lett.* **110**, 206403 (2013).
- Schneider, C. *et al.* An electrically pumped polariton laser. *Nature* **497**, 348–352 (2013).

24. Tischler, J. R., Bradley, M. S., Bulovic, V., Song, J. H. & Nurmikko, A. Strong coupling in a microcavity LED. *Phys. Rev. Lett.* **95**, 036401 (2005).
25. Shi, L. *et al.* Spatial coherence properties of organic molecules coupled to plasmonic surface lattice resonances in the weak and strong coupling regimes. *Phys. Rev. Lett.* **112**, 153002 (2014).
26. Shirakawa, H., Louis, E. J., MacDiarmid, A. G., Chiang, C. K. & Heeger, A. J. Synthesis of electrically conducting organic polymers: Halogen derivatives of polyacetylene, (CH). *Chem. Commun.* **16**, 578–580 (1977).
27. Tang, C. W. & VanSlyke, S. A. Organic electroluminescent diodes. *Appl. Phys. Lett.* **51**, 913–915 (1987).
28. Burroughs, J. H. *et al.* Light emitting diodes based on conjugated polymers. *Nature* **347**, 539–541 (1990).
29. Kim, C., Burrows, P. E. & Forrest, S. R. Micropatterning of organic electronic devices by cold-welding. *Science* **288**, 831–833 (2000).
30. Forrest, S. R. The path to ubiquitous and low-cost organic electronic appliances on plastic. *Nature* **428**, 911–918 (2004).
31. Kahn, A., Koch, N. & Gao, J. Electronic structure and electrical properties of interfaces between metals and p-conjugated molecular films. *Polym. Sci. Polym. Phys.* **41**, 2529–2548 (2003).
32. Sirringhaus, H., Bird, M., Richards, T. & Zhao, N. Charge transport physics of conjugated polymer field-effect transistors. *Adv. Mater.* **22**, 3893–3898 (2010).
33. Arias, A. C., Mackenzie, J. D., McCulloch, I., Rivnay, J. & Salleo, A. Materials and applications for large area electronics: Solution-based approaches. *Chem. Rev.* **110**, 3–24 (2010).
34. Yan, H. *et al.* A high mobility electron transporting polymer for printed transistors. *Nature* **457**, 679–687 (2009).
35. Jones, B. A. *et al.* High-mobility air-stable n-type semiconductors with processing versatility: Dicyanoperylene-3,4,9,10-bis (dicarboximides). *Angew. Chem. Int. Ed.* **116**, 6523–6526 (2004).
36. Jones, B. A., Facchetti, A., Wasielewski, M. R. & Marks, T. J. Tuning orbital energetics in arylene diimide semiconductors. Materials design for ambient stability of n-type charge transport. *J. Am. Chem. Soc.* **129**, 15259–15278 (2007).
37. Ebbesen, T. W., Lezec, H. J., Ghaemi, H. F., Thio, T. & Wolff, P. A. Extraordinary optical transmission through sub-wavelength hole arrays. *Nature* **391**, 667–669 (1998).
38. Rodrigo, S., García-Vidal, F. J. & Martín-Moreno, L. Influence of material properties on extraordinary optical transmission through hole arrays. *Phys. Rev. B* **77**, 075401 (2008).
39. Przybilla, F., Genet, C. & Ebbesen, T. W. Long vs. short-range orders in random subwavelength hole arrays. *Opt. Express* **20**, 4697–4709 (2012).
40. Archambault, A., Marquier, F., Greffet, J.-J. & Arnaud, C. Quantum theory of spontaneous and stimulated emission of surface plasmons. *Phys. Rev. B* **82**, 035411 (2010).
41. Lagendijk, A., van Tiggelen, B. & Wiersma, D. S. Fifty years of Anderson localization. *Phys. Today* **62**, 24–29 (August, 2009).
42. Feist, J. & García-Vidal, F. J. Extraordinary exciton conductance induced by strong coupling. *Phys. Rev. Lett.* **114**, 196402 (2015).
43. Schachenmayer, J., Genes, C., Tignone, E. & Pupillo, G. Cavity-enhanced transport of excitons. *Phys. Rev. Lett.* **114**, 196403 (2015).
44. Kibis, O. V. How to suppress the backscattering of conduction electrons? *Europhys. Lett.* **107**, 57003 (2014).
45. Morina, S., Kibis, O. V., Pervishko, A. A. & Shelykh, I. A. Transport properties of a two-dimensional electron gas dressed by light. *Phys. Rev. B* **91**, 155312 (2015).

### Acknowledgements

This work was supported in part by USIAS, the ERC through the projects Plasmonics (227557), Suprafunction (257305), and Coldsim (307688), the International Center for Frontier Research in Chemistry (icFRC, Strasbourg), the ANR Equipex Union (ANR-10-EQPX-52-01), the Labex NIE projects (ANR-11-LABX-0058 NIE) and CSC (ANR-10-LABX-0026 CSC) within the Investissement d'avenir program ANR-10-IDEX-0002-02, RYSQ, as well as the NSF (PIF-1211914 and PFC-1125844), EOARD (FA8655-13-1-3032) and the Austrian Science Fund (FWF) via the project P24968-N27. Computations made use of the Janus supercomputer, supported by NSF (CNS-0821794), NCAR and CU Boulder/Denver.

### Author contributions

T.W.E. conceived the idea and supervised the project. T.W.E. and E.O. designed the device experiments. J.G., J.A.H. and E.D. undertook the spectroscopic experiments. E.D., E.O., J.G., J.A.H. and J.F.D. fabricated and performed the device experiments. B.D., P.S., C. Genet and E.S. helped with the interpretation of the experimental data. G.P., C. Genes and J.S. developed the theoretical framework and performed the simulations. All authors contributed to the discussions and the preparation of the manuscript.

### Additional information

Supplementary information is available in the [online version of the paper](#). Reprints and permissions information is available online at [www.nature.com/reprints](http://www.nature.com/reprints). Correspondence and requests for materials should be addressed to T.W.E.

### Competing financial interests

The authors declare no competing financial interests.

## Methods

**Two- and three-terminal devices including nanohole arrays.** All the electrodes were realized on a glass substrate BK7 (25 × 25 mm) after standard cleaning procedures with sonication in Alconox solution (0.8% solution in milliQ water), then rinsed with water and sonicated for 1 h in (spectroscopically pure) ethanol. The glass substrates were then dried in an oven overnight. Ag and Al electrodes (100 nm) were fabricated using an electron beam evaporator (Plassys ME 300) at optimized working pressure ( $\sim 10^{-6}$  mbar) and deposition rates ( $\sim 0.4$  nm  $s^{-1}$ ). Plasmonic hole arrays were generated by the NPVE software program and milled using a Carl Zeiss Auriga FIB system. 0.5 wt% of PDI2EH-Br<sub>2</sub> or 0.5 wt% of PDI2EH-CN<sub>2</sub>, or 1 wt% P(NDI2OD-T2) solutions were prepared by dissolving the molecules in spectroscopic grade anhydrous chloroform in an inert atmosphere and spin-coating onto the electrodes at 750 r.p.m., 1,000 r.p.m. and 4,000 r.p.m., respectively, to achieve 100-nm-thick films.

Regarding the fabrication of field-effect transistor devices starting from electrode pairs bearing nanohole arrays, the two-terminal structures described above were completed by spin-coating of a commercial fluoropolymer (Cytop 809-M) at 2,500 r.p.m., leading to 700-nm-thick dielectric layers. The dielectric layer, processed from an orthogonal solvent which prevents the underlying PDI film from dissolving, would act as the gate insulator for a three-terminal device whose fabrication was completed by thermal evaporation ( $P \sim 10^{-6}$  mbar, evaporation rate  $\sim 1$  nm  $s^{-1}$ ) of a 60-nm-thick Al gate at the top (see Fig. 3c). Mobilities and threshold voltage values were extracted as detailed later in this section.

The electrical characterization of both two- and three-terminal devices was carried out by means of a Cascade Microtech MPS probe station equipped with micro-positioners to contact the electrode pads. The  $I$ - $V$  (two-terminal device) and  $I_D$ - $V_G$  (three-terminal device,  $I_D$  drain current,  $V_G$  gate voltage) characteristics are recorded by means of a Keithley 2636A sourcemeter interfaced with LABTRACER 2.0 software. All the experiments were repeated more than six times and the current enhancement is plotted based on averaged and different runs, as shown in Fig. 2.

### Classical electrical characterization of the materials encompassed in this study.

Organic thin-film transistors were prepared starting from  $n^{++}$ -Si/SiO<sub>2</sub> substrates exposing pre-patterned interdigitated gold source and drain electrodes (purchased by the IPMS Fraunhofer Institute). After thorough cleaning by sonication in acetone and isopropanol, the substrates underwent a hexamethyldisilazane (HMDS, purchased from Sigma-Aldrich) treatment, which helps improve the surface quality and passivate possible electron trap states due to the hydroxyl

groups of the silanols (Si-OH) present at the silicon oxide surface. Afterwards, solutions of the different materials were spincoated onto the substrates, which were then used for electrical characterization (performed in an inert environment) by means of a Keithley 2636A electrometer interfaced with LABTRACER software.

**Ambient photoelectron spectroscopy measurements.** Ambient photoelectron spectroscopy measurements were performed by sampling in each measurement an area of about 4 mm<sup>2</sup> (beam size) using a photoelectron yield spectrometer operating in ambient environment (PYSA), Model AC-2 from Riken Keiki. The semiconductor films were prepared by spin-coating onto a conductive Au/glass substrate, which forms a film exceeding 10 nm and therefore sufficient to ensure that only the top material was probed.

The metal Al and Ag films on glass substrates were prepared as previously described and measured over time to determine whether the exposure to air would affect their respective work functions. The exposure of all metal films employed as electrodes in the electrical characterization measurements is minimized, amounting to some minutes in total, including the transfer time from the evaporating chamber into the FIB chamber (ultrahigh vacuum at  $10^{-6}$  mbar) and then into the glovebox (nitrogen).

The ionization energy of P(NDI2OD-T2) amounted to  $5.55 \pm 0.05$  eV, in perfect accordance with previous measurements<sup>46</sup>. By considering an optical band gap of 1.55 eV, as reported in ref. 47, it was possible to estimate the energy of the LUMO level of P(NDI2OD-T2) as  $4.00 \pm 0.05$  eV.

The ionization energy measured on Al and Ag films corresponds to their absolute work function. For Al films, the work function was found to be constant with time with a value of  $4.2 \pm 0.05$  eV. For Ag films, the variation of the work function over a period of time up to four days was monitored. The work function changed from 4.72 eV (fresh sample) up to 4.81 eV (3 days 14 h) which, including the experimental error (normally about 50 meV), gives a net variation of approximately 50 meV. The Ag work function was found to be 4.75 eV after some minutes of exposure to air, which most probably corresponds to the value the Ag work function during the device experiments.

## References

46. Yan, H. *et al.* A high-mobility electron-transporting polymer for printed transistors. *Nature* **457**, 679–686 (2009).
47. Mori, D. *et al.* Highly efficient charge-carrier generation and collection in polymer/polymer blend solar cells with a power conversion efficiency of 5.7%. *Energy Environ. Sci.* **7**, 2939–2943 (2014).